



Lipid topology and electrostatic interactions underpin lytic activity of linear cationic antimicrobial peptides in membranes

David J. Paterson^a, Manlio Tassieri^a, Julien Reboud^a, Rab Wilson^a, and Jonathan M. Cooper^{a,1}

^aDivision of Biomedical Engineering, School of Engineering, University of Glasgow, Glasgow G12 8LT, United Kingdom

Edited by David A. Weitz, Harvard University, Cambridge, MA, and approved August 7, 2017 (received for review March 20, 2017)

Linear cationic antimicrobial peptides are a diverse class of molecules that interact with a wide range of cell membranes. Many of these peptides disrupt cell integrity by forming membrane-spanning pores that ultimately lead to their death. Despite these peptides high potency and ability to evade acquired bacterial drug resistance, there is a lack of knowledge on their selectivity and activity mechanisms. Such an understanding would provide an informative framework for rational design and could lead to potential antimicrobial therapeutic targets. In this paper, we use a high-throughput microfluidic platform as a quantitative screen to assess peptide activity and selectivity by precisely controlling exposure to vesicles with lipid compositions that mimic both bacterial and mammalian cell membranes. We explore the complexity of the lipid–peptide interactions governing membrane-disruptive behaviors and establish a link between peptide pore formation and both lipid–peptide charge and topological interactions. We propose a topological model for linear antimicrobial peptide activity based on the increase in membrane strain caused by the continuous adsorption of peptides to the target vesicle coupled with the effects of both lipid–peptide charge and topographical interactions. We also show the validity of the proposed model by investigating the activity of two prototypical linear cationic peptides: magainin 2 amide (which is selective for bacterial cells) and melittin (which targets both mammalian and bacterial cells indiscriminately). Finally, we propose the existence of a negative feedback mechanism that governs the pore formation process and controls the membrane’s apparent permeability.

antimicrobial peptides | microfluidic | giant unilamellar vesicle | magainin | melittin

The emergence of drug-resistant bacteria presents a pressing challenge to medicine (1, 2). New therapeutic compounds are needed to break the cycle of resistance that occurs after the introduction of new antibiotics (3, 4). Linear cationic antimicrobial peptides (LCAMPs) are potential antibiotic candidates, with many of them showing high potency against Gram-negative and Gram-positive bacteria at low micromolar concentrations (5). They are particularly interesting, as they are immune from bacterial drug resistance mechanisms (5, 6). The classes of LCAMPs are diverse, with over 1,000 members expressed in widely separated taxonomic groups and characterized by their amphipathic and cationic membrane-bound helices (7–9). Unlike most peptide families, it is the physiochemical properties of the LCAMPs’ assembled helices, which render them homologous, rather than their amino acid sequence (10, 11). Some LCAMPs are selective for bacterial cells [e.g., magainin 2 amide (m2a) from the African clawed frog *Xenopus laevis* (8)]. Others target bacterial and mammalian cells indiscriminately [e.g., melittin from the venom of the bee *Apis mellifera* (9)].

Although many complex lipid–peptide interactions involving, for example, electrostatics and peptide hydrophobic moments have been proposed to influence their behavior (12, 13), a full understanding of the relationship between LCAMPs and the cell’s membrane is not complete (6, 7). One mechanism widely used to describe LCAMP behavior is the Shai–Matsuzaki–Huang

(SMH) model shown in Fig. 1 *A–E* (6, 14). Briefly, LCAMPs display random coil conformations in aqueous environments before spontaneously binding to lipid bilayers, where they adopt an amphipathic helical configuration. The peptides initially insert parallel to the membrane plane, leading to membrane thinning, as LCAMP helices increase their outer leaflet volume (7, 8, 14). After a threshold concentration of membrane-bound peptide is achieved, membrane integrity becomes compromised through a variety of peptide-induced effects (PIEs), including bursting, a detergent-like carpet mechanism, and formation of membrane-spanning toroidal pores (7, 9, 15, 16). The latter is marked by a shift in helical orientation (from parallel to perpendicular to the membrane plane) and by translocation of lipid and peptide material from the outer to the inner membrane leaflet. Although the SMH model provides a basic mechanistic framework for LCAMP activity, it cannot predict peptide activity within specific membrane systems (e.g., it is not able to explain LCAMP selectivity between bacterial and mammalian membranes, which are characteristically different in both charge and topology) (Fig. 1*F*).

Bacterial cells contain high proportions of anionic and conical geometry nonbilayer lipids, whereas the outer leaflets of mammalian membranes are zwitterionic with a neutral curvature profile (17, 18). These marked differences in membrane charge and topology are reflected in the physiochemical properties of two LCAMPs, the selective m2a and the nonselective melittin (Figs. 1*G* and 2). The cationic residues of m2a are distributed along its length in close proximity to three sterically active phenylalanine residues and form a large angle on the helical face (19). The wide polar angle renders m2a unable to fully insert into the hydrophobic core of lipid bilayers, acting as a membrane “wedge” that induces

Significance

We propose a mechanistic framework that explains the activity and selectivity of an important class of compounds known as linear cationic antimicrobial peptides. These molecules have the potential to be developed into highly potent and selective pharmaceuticals, as they are able to discriminate between mammalian and bacterial membranes, and so destroy pathogens. By comparing both selective and nonselective peptides, we show that their activity is governed by topological and electrostatic interactions between the membrane-bound peptide and the surrounding lipids. This framework could underpin strategies for the rational design of therapeutic agents that are potentially able to bypass the mechanisms of acquired bacterial drug resistance.

Author contributions: D.J.P. and J.M.C. designed research; D.J.P. and R.W. performed research; M.T. developed the analytical tool; D.J.P., M.T., and J.R. analyzed data; and D.J.P., M.T., J.R., and J.M.C. wrote the paper.

The authors declare no conflict of interest.

This article is a PNAS Direct Submission.

¹To whom correspondence should be addressed. Email: jon.cooper@glasgow.ac.uk.

This article contains supporting information online at www.pnas.org/lookup/suppl/doi:10.1073/pnas.1704489114/-DCSupplemental.

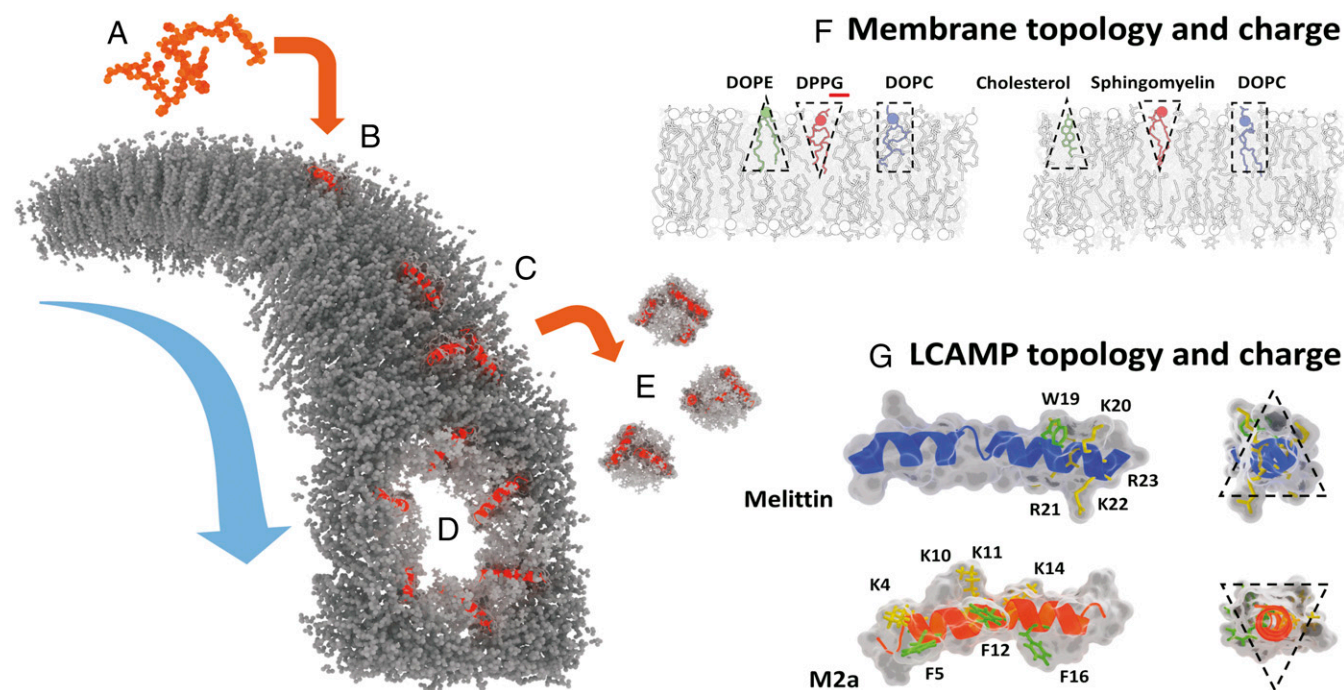


Fig. 1. The SMH model of LCAMP activity in lipid bilayers (gray). (A) LCAMPs (orange) bind to the outer membrane leaflet as amphipathic helices (B). Membrane-bound peptides (C) produce a variety of effects, including toroidal pore formation (D) and the release of lipid–peptide micelles in a detergent-like carpet mechanism (E). (F) Bacterial and mammalian membranes are characteristically different in charge and lipid topology. Bacterial outer leaflets contain lipids with large anionic head groups (e.g., DPPG) and conical nonbilayer lipids (e.g., DOPE), giving them a negative net charge and curvature profile. Mammalian outer leaflets contain bilayer lipids, like sphingomyelin, along with the conical geometry cholesterol, a lipid completely absent from bacterial membranes. They are net neutral in charge and curvature profile. (G) Similarly, melittin (blue) and m2a (orange) vary in charge and topological character. The four cationic lysines (K; yellow) and three phenylalanines (F; green) of m2a are distributed along its length, while the cationic arginines (R; yellow) and lysines (K; yellow) of melittin are clustered at the C terminus along with its single tryptophan residue (W; green). Melittin acts as a negative curvature membrane wedge (conical geometry), while m2a acts as a positive curvature wedge (inverse conical geometry).

positive curvature (9, 10). In contrast, melittin has a single sterically active tryptophan near its C terminus, where it clusters with its cationic residues, with a narrow polar angle formed on its helical face (7, 19). Melittin acts as a negative curvature-inducing membrane wedge owing to the deep penetration of its helix into the lipid bilayer (20). We now show that these inherent differences in lipid and peptide charges and topologies underpin LCAMPs activity and their selectivity between mammalian and bacterial cells.

We have used giant unilamellar vesicles (GUVs) as model systems of cell membranes. GUVs with different lipid topology and charge but with comparable size and curvature to mammalian cells are exposed to LCAMP within a high-throughput microfluidic device (Fig. S14). Dye leakage experiments have been used for the investigation of lipid–peptide interactions (21, 22). We have previously used such a technique within a microfluidic platform to precisely control the exposure of GUVs to LCAMPs (23). An advantage of this approach is the greatly increased experimental throughput over conventional techniques, which typically study only one GUV at a time.

By generating extensive dye leakage datasets (e.g., Fig. S2) from over 1,500 GUVs with different lipid compositions, we are able to gain insights into lipid–peptide topology and electrostatic interactions that are consistent with the existing SMH model. In particular, we provide not only a mechanistic explanation of LCAMP activity and selectivity but also, a predictive framework for peptide action within specific membranes. We show that the diverse membrane-disruptive activity of LCAMPs can be explained through both the accumulation of membrane strain and the relationship between lipid and peptide shape and charge. This extended model describes the selectivity mechanism of m2a for bacterial over mammalian cells as well as the nonselective

nature of melittin (8, 9). Finally, we propose a negative feedback mechanism within the pore formation process that controls the membranes' apparent permeability.

Results

We describe the effects of lipid charge and topological character on overall LCAMP lipid clustering and activity as well as the classification of PIEs and the dynamics of pore-mediated dye leakage.

Activity. Overall LCAMP activity was determined by the relationship between peptide and lipid topology with m2a and melittin activity arising in systems with opposing lipid geometries (Tables 1 and 2). Membrane-bound proteins form dynamic lipid rafts shown to be capable of preferentially associating with specific lipids, including cholesterol and sphingolipids (24). Fig. 2 shows the expected lipid associations of both m2a and melittin within all seven membrane compositions investigated (A–G), with consideration given to four factors.

- i) Membrane curvature. This is a modulator of lipid and protein localization as membranes seek to minimize free energy through reduction of their internal packing strain (25–27). By considering the established ability of melittin and m2a to induce opposing curvature in similar membranes, the peptides minimize packing frustration around them by clustering with lipids opposing the peptide-induced curvature (9, 15, 20). For example, membrane systems B and C contain positive curvature lipids [dipalmitoyl-phosphatidylcholine (DPPC)] that oppose melittin's negative curvature induction (i.e., they lower raft energy by clustering around the peptide helix).

A Lipid associations of m2a

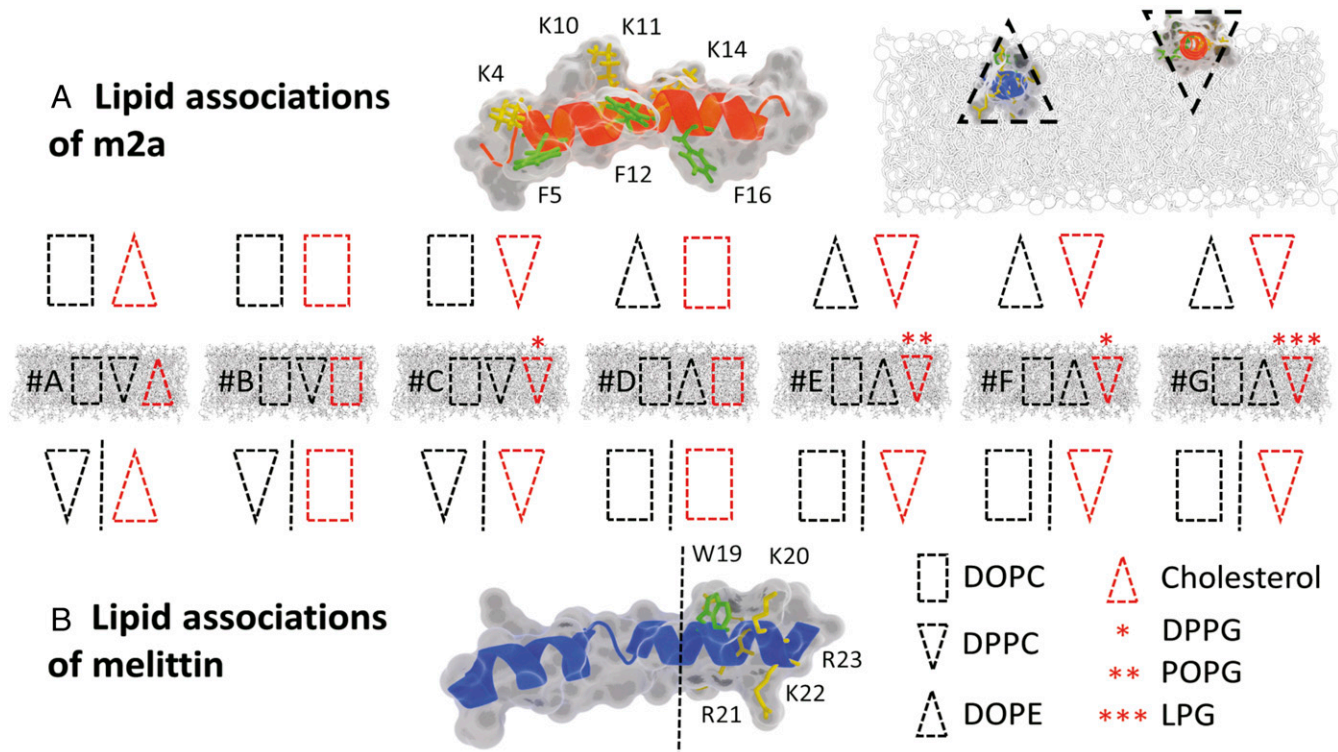


Fig. 2. The lipid associations of melittin and m2a in the membrane systems A–G, with lipid topology indicated by the block shapes. A red outline indicates lipids with a clustering mechanism either via electrostatics for the anionic lipids or via aromatic π -stacking with phenylalanine (F) and tryptophan (W) for cholesterol. (A) The block shapes indicate the topology of the lipids expected to associate with m2a. (B) The lipid topologies expected to associate with melittin. Shapes to the left of the dashed line associate with the peptides' helical face, while those to the right cluster with the peptides' tryptophan and cationic residues at the C terminus. (A, Top Right, Inset) The deeper penetration of melittin into the outer leaflet allows it to act as a negative curvature membrane wedge, while the shallower penetration of m2a results in a positive curvature wedge effect indicated by the appropriate block shapes.

- ii) Aromatic interactions. It is known that cholesterol forms π -stacking interactions with tryptophan and phenylalanine residues (28, 29). Here, cholesterol can cluster with phenylalanine residues of m2a and the sole tryptophan of melittin. The aromatic interactions bring a negative curvature lipid into contact with LCAMPs in the mammalian biomimetic membrane (system A).
- iii) Electrostatic interactions. These are powerful mediators of lipid–LCAMP associations (12). For example, system G contains the anionic lipid lysophosphoglycerol (LPG), which will form clusters around the cationic residues of both peptides.
- iv) Residue distribution. The positioning of cationic and sterically bulky residues affects lipid distribution around the helix (12, 28, 29); m2a distributes these residues along its helical length, and the lipids that associate with them (i.e., anionic lipids and cholesterol) will also locate along its helical length (Fig. 2).

Melittin isolates these residues at the C terminus, and anionic lipids and cholesterol will similarly locate there, leaving the helical face to associate with other lipid components.

These four factors underpin LCAMP activity, which we describe in more details in the following sections. Anionic lipids with low hydrophobic volumes and inverse conical geometry will activate m2a. For example, membrane systems C [dipalmitoyl-phosphoglycerol (DPPG)], F (DPPG), and G (LPG) contain inverse conical anionic lipids with saturated 16:0 palmitoyl fatty acids and return activities of 49, 72, and 51%, respectively. Substituting DPPG with 1-palmitoyl-2-oleoyl-phosphoglycerol (POPG; i.e., replacing a palmitoyl chain with an unsaturated 18:1; 9Z oleic chain) results in a fourfold decrease in activity between membranes F (DPPG: 72%) and E (POPG: 16%). Conversely, lipids with large hydrophobic volumes

Table 1. PIEs of the LCAMP melittin

System	Composition	No effect (%) \pm SD	Pore (%) \pm SD	Burst (%) \pm SD	Carpet (%) \pm SD	Other (%) \pm SD
A	DOPC:DPPC:chol	0	37 \pm 7	22 \pm 4	40 \pm 10	1 \pm 2
B	DOPC:DPPC:DOPG	3 \pm 4	58 \pm 13	3 \pm 3	30 \pm 12	6 \pm 7
C	DOPC:DPPC:DPPG	22 \pm 13	54 \pm 6	10 \pm 6	10 \pm 11	4 \pm 4
D	DOPC:DOPE:DOPG	0	17 \pm 12	33 \pm 17	47 \pm 8	2 \pm 3
E	DOPC:DOPE:POPG	32 \pm 12	22 \pm 12	43 \pm 14	2 \pm 3	2 \pm 3
F	DOPC:DOPE:DPPG	31 \pm 12	14 \pm 7	39 \pm 10	13 \pm 11	3 \pm 6
G	DOPC:DOPE:LPG	27 \pm 17	19 \pm 2	27 \pm 9	18 \pm 7	9 \pm 6

PIEs of LCAMP melittin in membrane systems A–G. Listed are the membrane compositions and the PIEs recorded for each lipids system after exposure to 1 μ M peptide, including no effect, pore-mediated leakage, carpet mechanism, and other. Each dataset is composed of at least 34 vesicles from at least three independent experiments, and the SD is included. Bold values are the results discussed within the text and are a guide to the eye only. chol, cholesterol.

Table 2. PIEs of the LCAMP m2a

System	Composition	No effect (%) \pm SD	Pore (%) \pm SD	Burst (%) \pm SD	Carpet (%) \pm SD	Other (%) \pm SD
A	DOPC:DPPC:chol	69 \pm 12	3 \pm 5	18 \pm 9	10 \pm 6	1 \pm 1
B	DOPC:DPPC:DOPG	82 \pm 6	7 \pm 2	6 \pm 5	0	6 \pm 8
C	DOPC:DPPC:DPPG	51 \pm 13	38 \pm 11	0	7 \pm 9	4 \pm 3
D	DOPC:DOPE:DOPG	94 \pm 6	0	3 \pm 3	3 \pm 3	0
E	DOPC:DOPE:POPG	84 \pm 5	0	2 \pm 5	9 \pm 7	5 \pm 10
F	DOPC:DOPE:DPPG	28 \pm 12	42 \pm 26	12 \pm 12	15 \pm 4	3 \pm 4
G	DOPC:DOPE:LPG	49 \pm 5	14 \pm 3	28 \pm 9	8 \pm 14	0

PIEs of LCAMP m2a in membrane systems A–G. Listed are the membrane compositions and the PIEs recorded for each lipids system after exposure to 1 μ M peptide, including no effect, pore-mediated leakage, carpet mechanism, and other. Each dataset is composed of at least 34 vesicles from at least three independent experiments, and the SD is included. Bold values are the results discussed within the text and are a guide to the eye only. chol, cholesterol.

[e.g., dioleoyl-phosphatidylcholine (DOPC), dioleoylphosphatidylethanolamine (DOPE), and 1,2-di-(9Z-octadecenoyl)-*sn*-glycero-3-phospho-(1'-*rac*-glycerol) (DOPG)] from their unsaturated 18:1 oleic fatty acid chains or cholesterol [a lipid with large negative curvature (18)] inactivate m2a. Indeed, membranes A (cholesterol), B (DOPG), and D (DOPG) return activities of 31, 18, and 6%, respectively. Similarly, within the context of topological constraints, melittin shows an opposing trend compared with m2a. Its activity is enhanced by interaction with large-hydrophobic volume lipids and reduced by the presence of inverse conical low-hydrophobic volume lipids. For instance, although melittin is generally more active than m2a, systems C (DPPC and DPPG), F (DPPG), and G (LPG) show the highest activities for m2a, whereas they yield low melittin activities of 78, 69, and 73%, respectively.

PIE Classification. m2a and melittin behavior can be further classified into three groups: pore-mediated leakage, where dye efflux occurs with no loss of membrane volume (7, 15, 16); a detergent-like carpet mechanism, where dye efflux is coupled to a loss of membrane volume (7, 9); and bursting, where dye loss is complete and instantaneous (Figs. S3–S7 and Movies S1–S3). Tables 1 and 2 report the percentage values of the PIEs recorded for the membrane systems A–G. It is clear that the two LCAMPs investigated vary widely in their membrane-disruptive behavior, even when tested using identical membranes. Below, we describe each of these leakage processes and build a correlation between them and their associated lipid–peptide interactions.

Pore Events. The three highest levels of melittin pore activity occur in systems A (37%), B (58%), and C (54%). Notably, they all contain the zwitterionic inverse conical lipid DPPC, which is expected to cluster along the peptides' helical face (Fig. 2). As LCAMP pore formation is coupled to a shift in peptide orientation from parallel to the membrane plane to perpendicular to it (14, 16) by inserting the center of the helix deep into the membrane core, it is likely that the pore rim is primarily composed of those lipids along the helical face. The opposite situation, where melittin clusters with high-hydrophobic volume lipids along its helical face (i.e., DOPC in systems D–G), produces low levels of pore activity: 17, 22, 14, and 19%, respectively. Pore formation is, therefore, favored by the presence of positive curvature lipids coupled to a clustering mechanism that will enrich these lipids along the helical face. m2a displays high levels of pore formation in systems C (38%) and F (42%), where the peptide will cluster with the positive curvature anionic lipid DPPG through electrostatic interactions with the cationic residues along the helical face. Membrane C presents the highest relative pore formation of any lipid–peptide system tested, with 78% of active GUVs displaying pore-mediated leakage events.

Carpet Events. Melittin displays a significant number of carpet events in systems A (40%), B (30%), and D (47%), where it as-

sociates with high-hydrophobic volume lipids at its C terminus either via electrostatic clustering with anionic conical geometry lipids or via π -stacking interactions between tryptophan and cholesterol (12, 28, 29) (Fig. 2). Conversely, our results (Tables 1 and 2) show that carpet events are suppressed when melittin clusters with low-hydrophobic volume lipids at its C terminus [i.e., POPG in system E (2%) and DPPG in systems C and F (10 and 13%, respectively)]. m2a displays its highest levels of carpet events when clustered with lipids matching its own positive curvature induction, returning 15% in system F (DPPG).

Bursting Events. Melittin displays its highest levels of vesicle bursting in lipid compositions D (33%), E (43%), and F (39%), where the peptide tends to form lipid rafts enriched with the high-hydrophobic volume lipid DOPC. Conversely, bursting is suppressed when melittin associates with lipids having low hydrophobic volumes [i.e., DPPC in systems A (22%), B (3%), and C (10%)]. m2a displays high levels of bursting in membranes where it forms rafts enriched with lipids having high hydrophobic volume [i.e., cholesterol and DOPC in membrane A (18%) and DOPE in membranes F and G (12 and 28%, respectively)]. Bursting events are also strongly disfavored in system with composition C (no bursting activity; of 59 GUVs observed), where m2a associates with the low-hydrophobic volume anionic lipid DPPG.

Pore-Mediated Efflux Dynamics. A subpopulation of dye efflux traces displays complex multimodal dynamics, with distinct changes in dye efflux over the timescale of the leakage process. Fig. 3A shows an example of a multimodal dye leakage trace for a system C vesicle (DOPC:DPPC:DPPG) after exposure to 1 μ M of m2a.

The data extracted from these dye efflux traces (Fig. 3B and C) show the existence of well-defined characteristic efflux rates when membranes are exposed to either melittin or m2a. The membranes' apparent permeability centers around a few common values for all of the explored systems as shown in Fig. 3D–F (see Fig. S8 for details on processing). A Shapiro–Wilks test was performed to show that the data were not a random sampling of a normal distribution to a high degree of confidence for all groupings ($P < 0.05$). This discretization phenomenon is not supported by the SMH model.

Discussion

As stated, Tables 1 and 2 support the hypothesis that lipid topology is an important modulator of LCAMP activity, with positive curvature lipids activating m2a and negative curvature lipids activating melittin. Here, we discuss in greater detail the impact of topological drivers on peptide activity and propose a model for LCAMP pore formation and selectivity.

Pore Formation. After their formation, lipid–LCAMP rafts diffuse laterally in the outer leaflet and create transient raft assemblies, which may form a membrane “hotspot”—a prepore region with increased packing frustration (30). To form a pore, the lipid–peptide

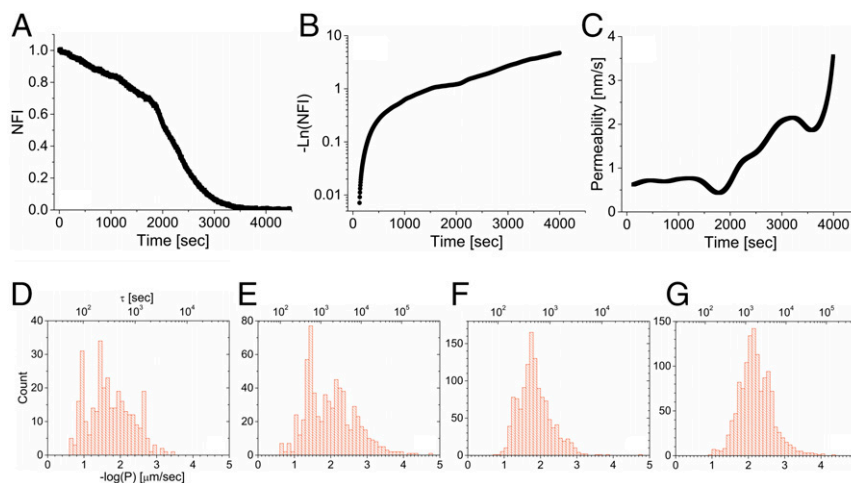


Fig. 3. (A) The normalized fluorescence intensity (NFI) function as a measure of the dye efflux of a system C *GUV* exposed to 1 μM LCAMP m2a. The trace displays multiple changes in leakage dynamics. (B) The $-\ln(\text{NFI})$ plot of the same trace shown in A. (C) This plot shows an example of the continuous change in membrane apparent permeability over the course of the entire leakage process from the data presented in A (as described in the *SI Materials and Methods*). D–G are the apparent membrane permeability histograms of (D) system A (mammalian biomimetic membrane) exposed to 1 μM m2a, which show the presence of distinct characteristic membrane flux rates or equivalently leakage characteristic times (τ ; top axis). (E) System C (bacterial biomimetic) vesicles exposed to 1 μM m2a. (F) System A exposed to 1 μM melittin featuring the presence of flux groupings, although less evident than the case with m2a. (G) System C *GUVs* exposed to 1 μM melittin.

system must reorganize from a bilayer into a higher energy, tightly curved structure. The pore formation process in peptide-free membranes under mechanical stress provides a useful framework to describe the energy difference (E_R) between pore-containing and pore-free membranes (31, 32). Based on the same principles, here we describe the interaction between LCAMPs and the membranes by means of Eq. 1:

$$E_R = \gamma 2\pi R - \left(\sigma_G \pi R^2 + \sum_{\pi R^2} E_L \right). \quad [1]$$

Eq. 1 shows the energy difference between pore-free and pore-containing membranes (E_R); γ is the pore rim line tension, R is the pore radius, σ_G is the bulk (global) membrane tension after LCAMP binding from solution, and $\sum_{\pi R^2} E_L$ is the sum of the energy produced by lipid–peptide interactions within the prepore region.

The term $\gamma 2\pi R$ represents the pore line tension, which will vary depending on the lipid composition of the membrane (26), while $\sigma_G \pi R^2$ is the work required to open the pore against membrane tension. The final term ($\sum_{\pi R^2} E_L$) represents the energy contained within the lipid–LCAMP rafts within the prepore region. When conditions reach $E_R < 0$, pore structures become thermodynamically favored. Lipid–LCAMP interactions affect all three terms of Eq. 1 and provide specific predictions from the topological model concerning LCAMP pore formation behavior as described below.

Pore Rim Line Tension ($\gamma 2\pi R$). Toroidal pores possess a tightly positively curved leaflet fold structure, where the inner and outer membrane leaflets bend into one another. Lipid curvature has been shown to stabilize and/or induce nanoscale membrane curvature, reducing lipid packing frustration (26).

The sterically bulky amino acid residues, phenylalanine and tryptophan, are key mediators of LCAMP activity, although their precise role during pore formation remains unknown (7). Within the topological model, we propose that phenylalanine and tryptophan act as positionally flexible membrane topology wedges that are able to shift position within the membrane and manipulate the topography of the surrounding lipids. The positioning

of one of these sterically bulky amino acids within the interfacial area of the outer leaflet increases the positive curvature of the adjacent lipids and favors pore formation through the stabilization of the leaflet fold structure (i.e., low γ value). Both phenylalanine and tryptophan residues are known to perform similar gating functions (shifting position within the membrane from the hydrophobic core to the interfacial region) for several transmembrane receptor proteins (33).

This process can be evaluated using the packing parameter (S), a metric which links lipid geometrical properties with their preferred supramolecular packing organization in aqueous environments (34). This measure is defined as $S = V/(a \times l)$, where V is the hydrocarbon volume, a is the head group area, and l is the hydrocarbon chain length. Fig. 4 shows this concept for m2a using three lipids in our dye leakage experiments (i.e., DOPE, DPPC, and DOPC). The new packing parameter, S^* , is calculated by adding the area of the main steric component of a phenylalanine residue [a benzene ring with a cross-sectional area of 40 \AA^2 (28)] to the head group area, a .

The conical nonbilayer lipid DOPE has a native S value of 1.41, forming inverse hexagonal phases in aqueous solution (34). When the head group area is occupied by the phenylalanine residues of m2a, the S value drops to 0.8, predictive of a bilayer system [$1.20 > S > 0.74$ is the requirement for stable bilayer formation (35)]. The cylindrical DOPC and the inverse conical DPPC possess native S values indicative of bilayer structures. In these cases, m2a forces S^* values below the bilayer threshold into geometries preferring hexagonal phase structures ($0.30 < S < 0.74$) (35). This packing change is of particular interest because of the similarities between the lipid packing of hexagonal phases and idealized toroidal pore structures (Fig. S9).

Given that pore formation is linked to peptide insertion parallel to the membrane normal, it is likely that the lipids along the helical face form the curved leaflet fold structure (7, 8). LCAMPs that associate with positive curvature lipids along their helical face produce low γ values, favoring pore formation, whereas in systems where the peptide associates with either neutral or negatively curved lipids, higher γ values are produced; consequently, pore formation is decreased.

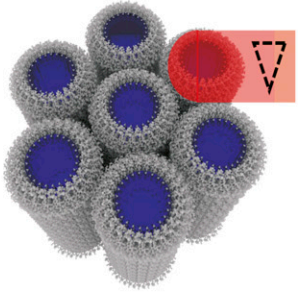
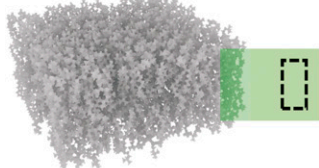
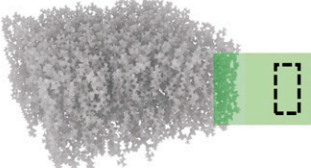
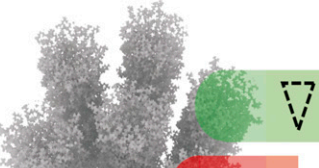
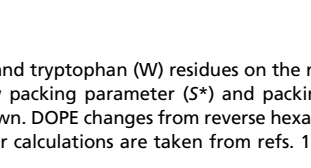
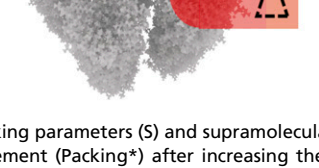
Lipid	S	Packing	F and W induced packing change	Packing*	S*	
DOPE	1.41	HII			Bilayer	0.80
DOPC	1.08	Bilayer			HI	0.68
DPPC	0.78	Bilayer			HI	0.53

Fig. 4. The effect of phenylalanine (F) and tryptophan (W) residues on the native packing parameters (S) and supramolecular packing arrangements of the lipids DOPE, DOPC, and DPPC. The new packing parameter (S*) and packing arrangement (Packing*) after increasing the lipid head group area by the phenylalanine sidechains of m2a are shown. DOPE changes from reverse hexagonal phase (HII) to bilayer packing, and DOPC and DPPC change from bilayer to hexagonal phase (HI) packing. Values for calculations are taken from refs. 17, 18, 20, 25, 35, and 38.

Work to Open a Pore ($\sigma_G \pi R^2$). This term is modified from previous work (31, 32) by making the membrane tension sensitive to LCAMP binding. During the continuous exposure of a vesicle to LCAMPs within the microfluidic device, peptides constantly bind to the outer leaflet, with the consequence of thinning and weakening the membrane (9) (i.e., σ_G continuously decreases with time) in proportion to the amount of membrane-bound LCAMP. Melittin inserts deep into the bilayer and results in a greater leaflet area asymmetry per peptide monomer than m2a (8, 20), providing a higher contribution toward σ_G and hence, an increased activity. Moreover, the topological model predicts that pore formation should be dependent on vesicle size caused by the inverse scaling of membrane tension with vesicle radius (36), which will alter σ_G . Consequently, a prediction of the topological model is that pores in small GUVs are harder to open than those in large GUVs, as they require greater work to open against their increased membrane tension. This is a marked departure from the established SMH model, which does not comment on vesicle size.

Lipid–Peptide Interaction Energy (E_L). LCAMPs surrounded by lipids with matching curvature properties will increase raft packing frustration (37) and generate high E_L . Within anionic (i.e., bacterial) membranes, these high-energy interactions can be forced via electrostatics (12). The topological model proposes that, for m2a, inverse conical anionic lipids (e.g., DPPG) can be brought into close proximity to the peptides' three phenylalanine (F) residues because of their close spatial relationship with the peptides' cationic lysine (K) residues (Fig. 2), specifically K4 and F5, K10/11 and F12, and K14 and F16. These large head group lipids will compete for interfacial area with the F residues of m2a, generating increased lipid–peptide packing frustration and increasing E_L . Conversely, melittin will generate large E_L values when surrounded by conical lipids owing to its induction of negative curvature.

Extended LCAMP Model. Here, based on our experimental results, we summarize our proposed topological model (Fig. 5 A–E), which adds both explanatory and predictive power to the SMH

model (Fig. 6). LCAMP behavior can be understood by means of simple concepts, namely lipid–peptide charge and topological interactions. The process is driven by the accumulation of strain within the target membrane through the occupation of outer leaflet volume by the LCAMP binding from solution. The precise nature of PIEs seen within a membrane is controlled by the charge and topological interactions occurring within the lipid–peptide rafts.

Overall activity is controlled by clustering with lipids that match the peptides' own curvature—negative (conical) and positive (inverse conical) curvatures for melittin and m2a, respectively (Fig. 5B), that generate high σ_G . The carpet mechanism is promoted by clustering with similar lipids at the C terminus of melittin and along the helical face of m2a (Fig. 5C), causing high E_L . The combination of peptide and lipid curvature can stabilize the tightly curved lipid–peptide micelles produced by the carpet mechanism. Bursting is favored by conical lipids for both peptides, although melittin associating with high-hydrophobic volume clustering lipids tends to react via the carpet mechanism, while m2a shows sensitivity to both clustering and nonclustering conical lipids (Fig. 5D). The data suggest that bursting occurs when the LCAMPs associate with lipids that disfavor other PIEs, such as clustering with high-hydrophobic volume lipids, which disfavor efficient leaflet fold packing, or with lipids opposing the peptides' own curvature induction, suppressing the carpet mechanism. Pore formation is favored via the association of inverse conical positive curvature lipids for both melittin and m2a (Fig. 5E). A negative feedback system between LCAMPs binding from solution and lipid–peptide transfer between leaflets through open pores governs peptide pore formation (Fig. 5 F–H).

Model Predictions. Using the patterns in lipid–peptide topological interactions and their effects on the terms of Eq. 1, it is possible to make general predictions concerning the PIE activity of LCAMPs within membrane systems of defined topology and charge (Fig. 6).

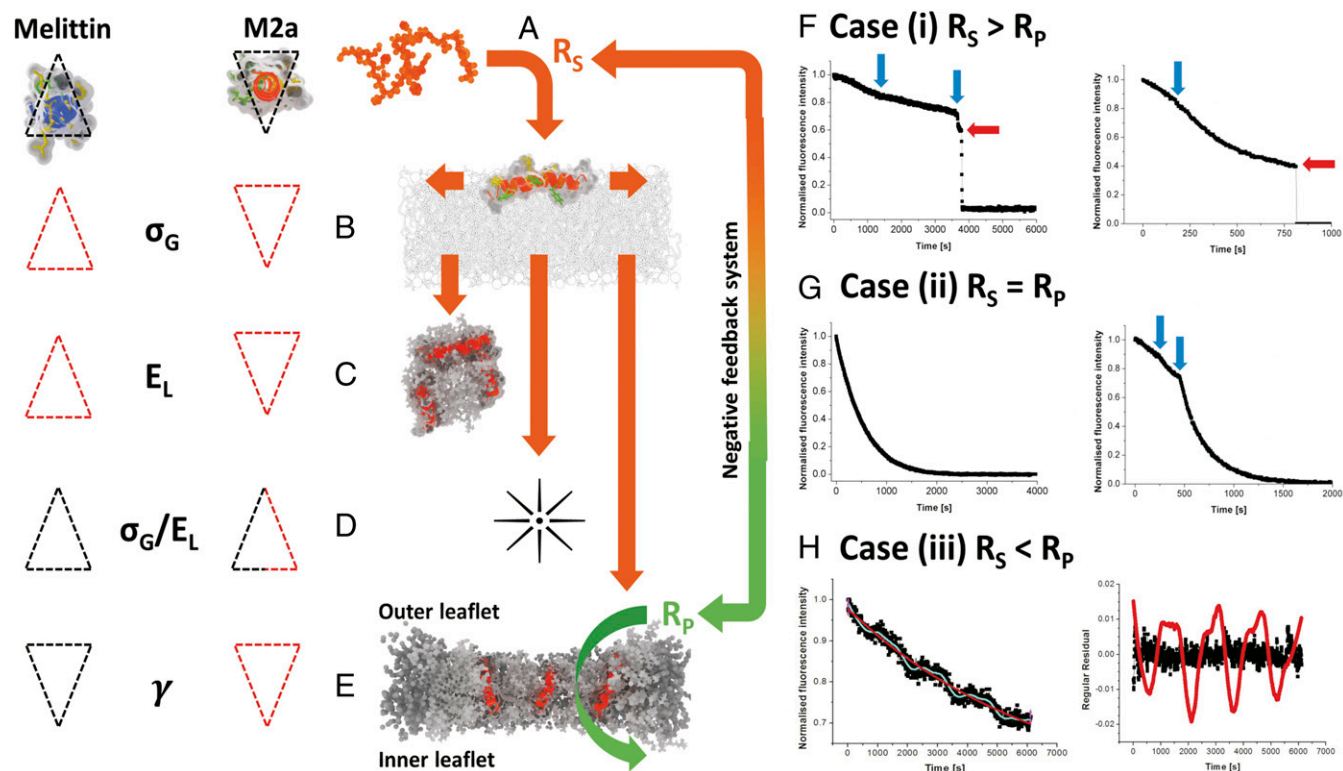


Fig. 5. (A) The topological model proposes that lipid–peptide shape and charge interactions govern the behavior of LCAMPs. *B–E* show the specific lipid clustering and geometries responsible for individual PIs, with lipid geometry shown using block shapes and clustering lipids given as a red outline. The terms of Eq. 1 associated with each PIE are also shown. (A) Peptide binds to the outer leaflet, generating internal membrane strain (σ_G), which controls overall activity (B). Both peptides are more active when clustered with lipids matching their own curvature strain: melittin with conical lipids and m2a with inverse conical lipids. (C) Clustering with lipids matching peptide curvature also governs the carpet mechanism by generating high E_L values and stabilizing the high-curvature lipid–peptide micelles produced. (D) Bursting events for melittin occur when the membrane contains nonclustering conical lipids, which will generate high E_L raft assemblies that cannot react via pore formation (high γ); instead, they cause complete vesicle failure. For m2a, both clustering and nonclustering conical lipids cause bursting. (E) Melittin generates pore activity (low γ) when inverse conical lipids associate with its helical face, while m2a generates pores when clustered with inverse conical lipids. Open pores allow interleaflet material transfer, lowering σ_G and generating a negative feedback system between the rate of LCAMP binding from solution (R_S) and the rate of material flow through open pores (R_P), with three possible cases. (i) $R_S > R_P$ shown in *F*; there is a continuous increase in σ_G , causing pore opening (blue arrows) until the membrane failure point is reached and the vesicle bursts (red arrows). Examples are shown for system A exposed to m2a (*F, Left*) and for system C for melittin (*F, Right*), which display complex leakage dynamics, as several pores open (blue arrows) before a stable leak is established. (ii) $R_S = R_P$, resulting in a stable leak (*G*), shown for system C for m2a (*G, Left*) and melittin (*G, Right*). (iii) $R_P > R_S$, decreasing σ_G and favoring pore closure. This renders $R_S > R_P$, increasing σ_G and reinitiating pore formation. This results in pore opening and closing cycles. *H, Left* shows a pore-cycling leakage trace (system F; m2a), with its smoothed average (light blue) and fitted single-exponential decay curve (red). (*H, Right*) The residual between the two curves shown in *H, Left* (red) compared with the residual for a stable case *ii* leak (black). The residual shows dynamic cycling between at least two different leakage rates, with intervals between the minima of 1,517, 1,512, and 1,611 s. Consistent cycle spacing is caused by the constant R_S within the microfluidic device.

Negative Feedback and Toroidal Pores. Pore leakage dynamics can be explained by the inclusion of a negative feedback system within the topological model (Fig. 5 *F–H*). Toroidal pores are dynamic structures facilitating lipid and peptide transfer between the membrane leaflets (7, 8, 22), which amounts to a membrane relaxation process, reducing leaflet area asymmetry. Each pore opening renders subsequent pore openings less likely, creating negative feedback between the rate of LCAMP binding from solution (R_S), the flow of the lipid–LCAMP material through open pores (R_P), and the energy needed to open a pore structure (σ_G). This framework leads to three possible outcomes, all of which are consistent with the leakage dynamics recorded for m2a and melittin (Fig. 5 *F–H*).

- i*) $R_S < R_P$. Leaflet asymmetry continually increases, allowing raft assemblies of lower total E_L to create pores (Fig. 5*F*). A cascade of pore formation occurs until the membrane failure is reached and the GUV bursts.
- ii*) $R_S = R_P$. When the rates are in equilibrium during the leakage process (Fig. 5*G*). Initially, R_S is higher than R_P , and as membrane tension increases, this causes pore formation and

increases R_P . When R_S and R_P are equal, a stable leakage state can occur.

- iii*) $R_P > R_S$. Loss of outer leaflet volume decreases the area asymmetry between the outer and inner leaflets, decreasing membrane tension and causing pore closure until $R_S > R_P$ and pore activity resumes. The negative feedback loop leads to cycles of high and low pore activity, as membrane tension repeatedly crosses the energy threshold required for lipid–LCAMP rafts to form pores (Fig. 5*H*).

We propose that this negative feedback explains the discretizing of LCAMP pore leakage behavior observed in Fig. 3, where leakage traces arrange in groups with similar dynamics, which are controlled by the pore size and number within the membrane (i.e., by their apparent permeability). We next apply the model to the selectivity mechanism of LCAMPs between mammalian and bacterial cells.

Implications for Selectivity. Deciphering and controlling selectivity is a key consideration in the development of antimicrobial agents, and our topological model provides a powerful tool to understand this process. To succeed as antimicrobial agents,

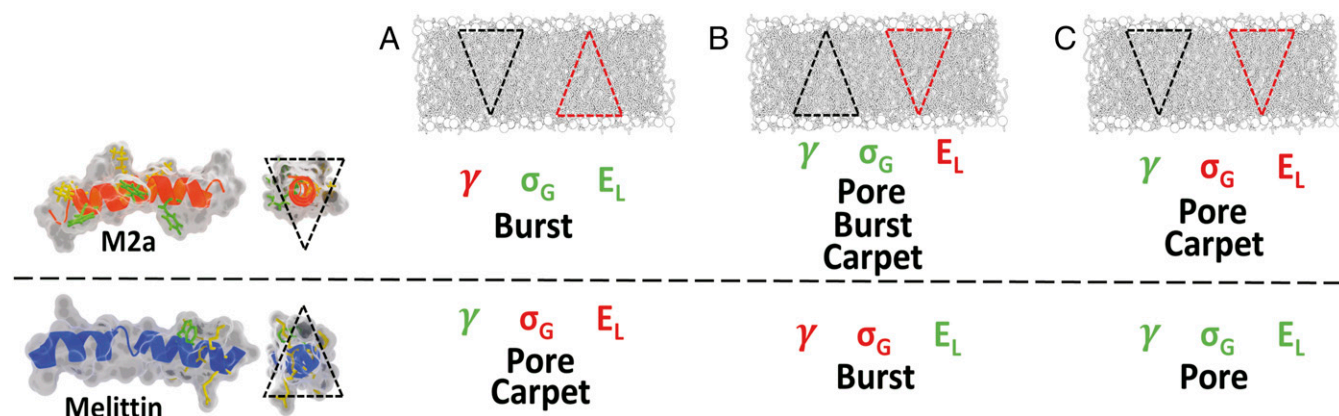


Fig. 6. Predictions for LCAMP behavior within membranes based on the lipid–peptide topological interactions and their effects on the terms of Eq. 1 (γ , pore rim line tension; σ_G , membrane tension; and E_L , lipid–peptide interaction energy). The lipid topology of the membrane systems is indicated by block shapes, with lipids having a clustering mechanism given as a red outline. Within A, m2a generates high γ values (red) but low σ_G and E_L (green) through clustering with conical lipids along its helical face. Pore mechanism is suppressed via inefficient leaflet fold packing, while carpet mechanism is suppressed by nullification of the peptides' positive curvature. m2a will, therefore, react via bursting. Melittin clusters the conical lipids at its C terminus and associates with the inverse conical lipids along its helical face. This generates low γ combined with high E_L at the C terminus and will respond via both pore (low γ) and carpet mechanisms (high E_L). (B) In this membrane, m2a clusters inverse conical lipids at its helical face, generating low γ and high E_L , which together with the presence of conical nonbilayer lipids allows the peptide to produce all three PIEs. Melittin generates higher γ and lower E_L and primarily reacts via bursting. (C) m2a produces low γ and high E_L through clustering with inverse conical lipids along its helical face. This will generate pore and carpet mechanisms. Melittin generates low γ and E_L and will be forced to react mainly via bursting.

LCAMPs must form pores in bacterial membranes (i.e., render $E_R < 0$), while leaving mammalian membranes intact ($E_R > 0$). Using our lipid systems as examples, we explore how the characteristic electrostatic and topological differences between bacterial and mammalian membranes affect the terms in Eq. 1, yielding important considerations for peptide selectivity.

The opposing charge and topological characters of the non-selective melittin and the selective m2a mean that, within identical membranes, they can form rafts enriched with different lipids (Fig. 2). The clustering of melittin's charged and sterically bulky residues at one end of the helix leaves the helical face free to interact with zwitterionic membrane components, making melittin more sensitive to zwitterionic lipid topology than m2a, which has cationic residues that are distributed along its helical length.

Bacterial outer membrane leaflets contain anionic lipids, many of which have large head groups and inverse conical geometries (12, 18). Electrostatic interactions can force these lipids into close contact with the helical face of m2a, favoring pore formation through efficient pore leaflet fold packing (i.e., low γ) and forcing unfavorable high E_L topological interactions. For example, in system C (DOPC:DPPC:DPPG), m2a is an efficient pore former, returning the highest relative ratio of pore activity (78%). Bacterial membranes also contain a large proportion of conical nonbilayer lipids, like DOPE (19), similar to Fig. 6B. These lipids induce membrane packing frustration into the bilayer. This lowers the barrier to pore formation (i.e., lower contribution from σ_G to render $E_R < 0$). Notably, pore formation by m2a in system F occurred faster than in any other membrane system tested (Tables S1 and S2), although the reduced positive curvature lipid content compared with system C produced lower relative pore formation (54%). *SI Materials and Methods* contains a more detailed discussion of the implications of the model for the timings of PIE initiation for membrane systems A–G.

Mammalian cells maintain zwitterionic outer membrane leaflets composed of bilayer lipids with large head groups, like phosphatidylcholine, and contain cholesterol (18), a membrane component completely absent from bacteria (similar to Fig. 6A). Within mammalian membranes, m2a is free from forced electrostatic interactions and can associate with lipids that minimize its raft energy (Fig. 2). m2a pore activity is notably suppressed in the

mammalian biomimetic membrane (system A), where the peptide is expected to form cholesterol-enriched rafts through π -stacking interactions with its phenylalanine residues (28, 29). This puts a negative curvature, high-hydrophobic volume lipid into association with the peptide, which will not efficiently pack the pores leaflet fold (i.e., high γ), both lowering raft energy (i.e., low E_L) and disfavoring pore formation. m2a was generally less active than melittin; however, in membranes with specific charge and topologies, it is capable of fast and efficient pore formation.

Conclusions

High-throughput analysis of dye leakage experiments of GUVs with different lipid compositions has enabled the in-depth study of the membrane-disrupting properties of LCAMPs. This has allowed us to propose the presence of a negative feedback system between membrane strain (σ_G) and pore opening that can be used to describe pore behavior. By using steric and electrostatic interactions as primary considerations, we have developed a model for LCAMP behavior that provides a predictive mechanism for activity and selectivity. The model has potential application in the rationale design of therapeutics, which are urgently required to combat the rapid spread of drug-resistant bacterial strains. By using the proposed models framework, LCAMPs can be designed to generate efficiently packed pores (low γ) together with high-leaflet area asymmetry (σ_G) and lipid–LCAMP interaction energy (E_L) within a variety of membranes, providing the opportunity of tailoring peptide activity to specific bacterial membranes. We propose that lipids must be considered involved participants in the membrane disruption caused by LCAMPs instead of being merely passive in the process.

Materials and Methods

The materials and methods are described in detail within *SI Materials and Methods*. Briefly, GUVs were formed by in situ electroformation within the microfluidic device from seven different lipid compositions (A–G) of varying topology and charge (see Table S3 for the composition of each system and Table S4 for the electroformation process parameters). System A is based on a typical mammalian membrane composition, and systems B–G are based on an *Escherichia coli* membrane, which is dominated by phosphatidylethanolamine (PE) and phosphoglycerol (PG) lipid species (38). Membrane topography

was varied by changing the proportions of 16:0 and 18:1 fatty acid chains of the PG species and exchanging the PE head group for the larger phosphatidylcholine (PC) head group.

A fluorescent marker (AlexaFluor488-3k dextran) was incorporated within the GUVs, which were captured within a microfabricated trap array. Trapped GUVs were exposed to either a nonselective LCAMP (melittin) or a selective LCAMP (m2a) using microfluidic dispensation to precisely control both the duration of exposure and the final peptide concentration. GUVs were imaged during LCAMP exposure using confocal microscopy (Zeiss LSM 510 Live) at a data capture frequency of 0.25 frames per second (23). Activity was defined by the proportion of GUVs showing PIs: pore-mediated leakage, bursting or carpet mechanism (defined as shown in Figs. S3–S7). Data were collated into

characteristic profiles describing the frequency (percentage) of each of the three behaviors within the seven lipid compositions (A–G).

ACKNOWLEDGMENTS. We thank Dr. Alasdair Clark (University of Glasgow) for SEM and the James Watt Nanofabrication Centre (University of Glasgow) for help with device fabrication. Research was funded by the Engineering and Physical Sciences Research Council Doctoral Training Centre (EPSRC DTC) Grant EP/F500424/1, Proxomics Grant EP/1017887/1, and Frontiers Grant EP/K038885/1. M.T. acknowledges Royal Academy of Engineering/EPSRC Fellowship 10216/101. J.R. acknowledges the University of Glasgow Lord Kelvin and Adam Smith Research Fellowship. J.M.C. acknowledges support from EPSRC Personal Fellowship EP/K027611/1 and a European Research Council Advanced Grant Bio-Phonics.

1. Cohen ML (2000) Changing patterns of infectious disease. *Nature* 406:762–767.
2. Center for Disease Control and Prevention (2013) Threat report: Antibiotic resistance threats in the United States (US Department of Health & Human Services, Atlanta), Technical Report CS239559-B.
3. Davies J (2006) Bacteria on the rampage. *Nature* 383:219–220.
4. Walsh C (2000) Molecular mechanisms that confer antibacterial drug resistance. *Nature* 406:775–781.
5. Al-Ani I, Zimmermann S, Reichling J, Wink M (2015) Pharmacological synergism of bee venom and melittin with antibiotics and plant secondary metabolites against multi-drug resistant microbial pathogens. *Phytomedicine* 22:245–255.
6. Zasloff M (2002) Antimicrobial peptides of multicellular organisms. *Nature* 415:389–395.
7. Raghuraman H, Chattopadhyay A (2007) Melittin: A membrane-active peptide with diverse functions. *Biosci Rep* 27:189–223.
8. Matsuzaki K, Sugishita K, Harada M, Fujii N, Miyajima K (1997) Interactions of an antimicrobial peptide, magainin 2, with outer and inner membranes of gram-negative bacteria. *Biochim Biophys Acta* 1327:119–130.
9. Bechinger B, Lohner K (2006) Detergent-like actions of linear amphipathic cationic antimicrobial peptides. *Biochim Biophys Acta* 1758:1529–1539.
10. Haney EF, Hancock RE (2013) Peptide design for antimicrobial and immunomodulatory applications. *Biopolymers* 100:572–583.
11. Oren Z, Shai Y (1997) Selective lysis of bacteria but not mammalian cells by diastereomers of melittin: Structure-function study. *Biochemistry* 36:1826–1835.
12. Epand RF, Maloy WL, Ramamoorthy A, Epand RM (2010) Probing the “charge cluster mechanism” in amphipathic cationic antimicrobial peptides. *Biochemistry* 49:4076–4084.
13. Dathe M, Wieprecht T, Nikolenko H, Bienert M (1997) Hydrophobicity, hydrophobic moment and angle subtended by charged residues modulate antibacterial and haemolytic activity of amphipathic helical peptides. *FEBS Lett* 403:208–212.
14. Shai Y (1999) Mechanism of the binding, insertion and destabilization of phospholipid bilayer membranes by K-helical antimicrobial and cell non-selective membrane-lytic peptides. *Biochim Biophys Acta* 1462:55–70.
15. Brogden KA (2005) Antimicrobial peptides: Pore formers or metabolic inhibitors in bacteria? *Nat Rev Microbiol* 3:238–250.
16. Yang L, Harroun TA, Weiss TM, Ding L, Huang HW (2001) Barrel-stave model or toroidal model? A case study on melittin pores. *Biophys J* 81:1475–1485.
17. van Meer G, de Kroon AIMP (2011) Lipid map of the mammalian cell. *J Cell Sci* 124:5–8.
18. Silhavy TJ, Kahne D, Walker S (2010) The bacterial cell envelope. *Cold Spring Harb Perspect Biol* 2:a000414.
19. Dathe M, Wieprecht T (1999) Structural features of helical antimicrobial peptides: Their potential to modulate activity on model membranes and biological cells. *Biochim Biophys Acta* 1462:71–87.
20. Batenburg AM, van Esch JH, de Kruijff B (1988) Melittin-induced changes of macroscopic structure of phosphatidylethanolamines. *Biochemistry* 27:2324–2331.
21. Ladokhin AS, Selsted ME, White SH (1997) Sizing membrane pores in lipid vesicles by leakage of coencapsulated markers. *Biophys J* 72:1762–1766.
22. Matsuzaki K, Yoneyama S, Miyajima K (1997) Pore formation and translocation of melittin. *Biophys J* 73:831–838.
23. Paterson DJ, Reboul J, Wilson R, Tassieri M, Cooper JM (2014) Integrating microfluidic generation, handling and analysis of biomimetic giant unilamellar vesicles. *Lab Chip* 14:1806–1810.
24. Hebbar S, et al. (2008) A fluorescent sphingolipid binding-domain peptide probe interacts with sphingolipids and cholesterol-dependent raft domains. *J Lipid Res* 49:1077–1089.
25. Callan-Jones A, Sorre B, Bassereau P (2011) Curvature-driven lipid sorting in biomembranes. *Cold Spring Harb Perspect Biol* 3:a004648.
26. Zimmerberg J, Koslov MM (2006) How proteins produce cellular membrane curvature. *Nat Rev Mol Cell Biol* 7:9–19.
27. Almeida PF, Pokorny A, Hinderliter A (2005) Thermodynamics of membrane domains. *Biochim Biophys Acta* 1720:1–13.
28. Fantini J, Barrantes FJ (2013) How cholesterol interacts with membrane proteins: An exploration of cholesterol-binding sites including CRAC, CARC, and tilted domains. *Front Physiol* 4:1–9.
29. Zhou X, Xu J (2012) Free cholesterol induces higher β -sheet content in A β peptide oligomers by aromatic interaction with Phe19. *PLoS One* 7:e46245.
30. Mahalka AK, Kinnunen PKJ (2009) Binding of amphipathic α -helical antimicrobial peptides to lipid membranes: Lessons from temporins B and L. *Biochim Biophys Acta* 1788:1600–1609.
31. Lee M-T, Chen F-Y, Huang HW (2004) Energetics of pore formation induced by membrane active peptides. *Biochemistry* 43:3590–3599.
32. Leontiadou H, Mark AE, Marrink SJ (2004) Molecular dynamics simulations of hydrophilic pores in lipid bilayers. *Biophys J* 86:2156–2164.
33. Kelkar DA, Chattopadhyay A (2006) Membrane interfacial localization of aromatic amino acids and membrane protein function. *J Biosci* 31:297–302.
34. Isrealachvili J, Mitchell J, Ninham B (1976) Theory of self-assembly of hydrocarbon amphiphiles into micelles and bilayers. *J Chem Soc Faraday Trans 2* 72:1525–1568.
35. Kumar VV (1991) Complementary molecular shapes and the additivity of the packing parameter of lipids. *Proc Natl Acad Sci USA* 88:444–448.
36. Karatekin E, et al. (2003) Cascades of transient pores in giant vesicles: Line tension and transport. *Biophys J* 84:1734–1749.
37. Schneggenburger PE, Beerlink A, Weinhausen B, Salditt T, Diederichsen U (2011) Peptide model helices in lipid membranes: Insertion, positioning, and lipid response on aggregation studied by X-ray scattering. *Eur Biophys J* 40:417–436.
38. Oursel D, et al. (2007) Lipid composition of membranes of *Escherichia coli* by liquid chromatography/tandem mass spectrometry using negative electrospray ionization. *Rapid Commun Mass Spectrom* 21:1721–1728.
39. Angelova M, Soleau S, Meleard P, Faucon JF, Bothorel P (1992) Preparation of giant vesicles by external A.C. electric fields. Kinetics and applications. *Prog Colloid Polym Sci* 89:127–131.
40. Estes DJ, Mayer M (2005) Giant liposomes in physiological buffer using electroformation in a flow chamber. *Biochim Biophys Acta* 17:152–158.
41. Wheaton SA, Lakshmanan A, Almeida PF (2013) Statistical analysis of peptide-induced graded and all-or-none fluxes in giant vesicles. *Biophys J* 105:432–443.
42. Durrant JD, Amaro RE (2014) Lipidwrapper: An algorithm for generating large-scale membrane models of arbitrary geometry. *PLOS Comput Biol* 10:e1003720.
43. Meng Y, Shukla D, Pande VS, Roux B (2016) Transition path theory analysis of c-Src kinase activation. *Proc Natl Acad Sci USA* 113:9193–9198.
44. Versace RE, Lazaridis T (2015) Modelling protein-micelle systems in implicit water. *J Phys Chem B* 119:8037–8047.